Received: 11 March 2020 | Revised: 25 April 2020 | Accepted: 8 May 2020

DOI: 10.1002/eqe.3291

WILEY

RESEARCH ARTICLE

Experimental and computational synergy for modelling an advanced gas-cooled reactor core under seismic excitation

Luiza Dihoru[1] | **Olafur Oddbjornsson**[2] | **Ben Cannell**[3] | **Adam J. Crewe**[1] | **Tony Horseman**[1] | **Matt Dietz**[1] | **Colin A. Taylor**[1]

[1]Department of Civil Engineering, University of Bristol, Bristol, UK

[2]EFLA Consulting Engineers, Reykjavik, Iceland

[3]Energy, Atkins, Bristol, UK

Correspondence
Luiza Dihoru, Department of Civil Engineering University of Bristol, Bristol, UK.
Email: luiza.dihoru@bristol.ac.uk

Funding information
EDF Energy, Grant/Award Number: PLEX7b/4840455398

Summary

The advanced gas-cooled reactors (AGRs) are the backbone of the United Kingdom's nuclear generation fleet, producing approximately 17% of the country's electricity. Their safety cases are supported by thorough inspection and monitoring of their graphite cores and extensive theoretical, analytical, and experimental studies. This paper presents a unique, highly innovative and technically challenging earthquake engineering project that has provided vital evidence to underpin the seismic safety assessments of the AGRs. Two modelling approaches, one experimental (a multilayer array physical model), and one numerical (a SOLFEC nonsmooth contact dynamics computational model) have been developed to investigate the seismic behaviour of an aged graphite core. The synergetic relationship between the two approaches is a product of insightful collaborative learning between the University of Bristol and Atkins, with the experiments providing material parameters and validation data and the computer simulations feeding array design and test schedule recommendations to the physical model. The predictive capabilities of the physical and the numerical models are tested by direct comparison and the good agreement between the results has increased the confidence in both. The model's versatility allows a variety of core scenarios to be tested that can explore in detail the AGR core behaviour in seismic conditions.

KEYWORDS

advanced gas-cooled reactor, modelling, nonsmooth contact dynamics, seismic testing

1 | INTRODUCTION

This paper presents one of the most complex shaking table experiments ever attempted, involving a 42,000-component rig with approximately 3,200 transducers and a novel distributed data acquisition system that yielded approximately 20 TB of data in approximately 4,800 seismic tests. This work addresses a problem that has never been encountered before, namely the seismic structural integrity effects of the anticipated progressive cracking of the thousands of hollow graphite bricks that make up an advanced gas-cooled reactor (AGR) core structure. AGRs are unique to the United

Kingdom. The first four reactors to be commissioned were at Hinkley Point B and Hunterston B in 1976 and are currently scheduled for decommissioning in 2023. There is no experience of operating these reactors to such ages. Consequently, assessments of future safety require first principle approaches and insightful collaborative learning across many stakeholders. AGR core modelling, both physical and computational, provides one of the few ways of anticipating the possible future performance of the AGRs. Nuclear power in the United Kingdom generates around a quarter of the country's electricity as of 2016, projected to rise to a third by 2035 (National Audit Office[1]). In the United Kingdom there are 14 AGRs and one pressurised water reactor (PWR) with a combined capacity of approximately 10 GW (electricity). The AGRs are the second generation of British gas-cooled nuclear reactors, using graphite as the neutron moderator and carbon dioxide as the coolant. The AGR cores comprise of a stacked array of tubular graphite bricks and interlocking keys forming the fuel and the control rod channels. The core graphite component assembly is designed to provide neutron moderation, allow movement of fuel and control rods, and allow gas flow for cooling. These functions must be maintained in normal operating conditions but also during any hazardous natural events, such as earthquakes. Current international standards require that a nuclear plant should be qualified against at least 0.1 g peak ground acceleration (PGA), while the operators require that their nuclear power stations can be reliably shut down and held down in the case of a more severe seismic event with a probability of exceedance of 10^{-4} per annum. As a component of the power plant safety case, the seismic capability of the AGRs is supported by an extensive theoretical, analytical, and experimental programme, to which the University of Bristol (UOB) and Atkins are key contributors. The seismic capability needs to be demonstrated throughout the stations' lives and needs to take account of the consequences of fast neutron irradiation and radiolytic oxidation for graphite component behaviour. These degradation processes, which include changes in geometry, strength, and the potential for differential shrinkage-induced cracking (i.e., cracking that occurs when the inner and the outer areas of a hollow brick shrink at different rates) need to be captured in modelling. The earliest physical model for seismic behaviour included a simple 9 × 9 brick array, employed by the National Nuclear Corporation in 1985. Several enhanced analytical methods and physical models for static and dynamic behaviour have been reported in the last decade.[2,3] Between 2008 and 2012, a quarter-scale near-full single layer 20-rings array model ("the single-layer array (SLA)") was developed at UOB[4] to explore the basic mechanics of the core system as a precursor for a more sophisticated modelling tool: the quarter-scale 8-layer-20-bricks-across AGR core model ("the multilayer array (MLA)").[5]

This paper will focus on the MLA modelling in physical experiments and in SOLFEC, an implicit software implementing the nonsmooth contact dynamics (NSCD) method. Compared with standard finite-element approaches, the efficient handling of multibody interactions makes SOLFEC particularly well-suited to AGR core modelling wherein thousands of components with millions of degrees of freedom (DOF) are subjected to dynamic excitation. The computational model that was built for the purposes of this paper will be referred to as SOLFEC for simplicity. A complex experimental programme combined with SOLFEC simulations was carried out by UOB and Atkins to characterise the MLA and test its capabilities of predicting the dynamic response of an AGR at quarter scale. In order to secure unimpeded insertion and removal of the fuel rods and control rods in and out of the core channels, there is a fundamental requirement to keep these channels within their straightness tolerance. The main objective of the MLA-SOLFEC programme was to assess the shape of the control rod/fuel rod channels during a seismic event for both intact and degraded model arrays (arrays containing model cracked bricks). The relationship between the numerical work and the experiments was a synergetic one, with the rig providing material parameters and validation data to the code and the code feeding back array response assessments and design recommendations to the rig (Figure 1). The results will be

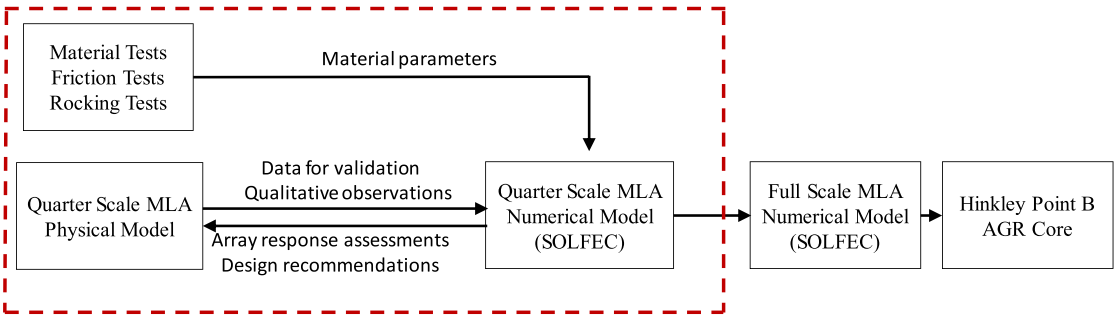

FIGURE 1 Workflow showing experimental and numerical work synergy (this paper covers the work shown in red box) [Colour figure can be viewed at wileyonlinelibrary.com]

employed, in the future, in full-scale numerical models to enable prototype AGR behaviour prediction. This paper focuses on the quarter-scale rig-SOLFEC comparison work.

2 | WORK OBJECTIVES

The MLA experimental programme was designed to investigate core array configurations (intact and cracked) in relevant seismic scenarios (i.e., site-specific seismic inputs for Hinkley Point B power station), with the main objective of providing data for computer model validation. The following strands of work were carried out for this purpose:

a Characterise the model material and the model components in the rig via material tests, component tests, and small array tests. Supply the required material properties to the numerical model.
b Analyse the features of the main numerical approaches, with particular emphasis on SOLFEC.
c Test the prediction capabilities of SOLFEC by direct comparison with the rig results and analyse the patterns of behaviour for the model array in intact and cracked conditions.

3 | QUARTER-SCALE PHYSICAL MODEL

The MLA rig (2.5 m wide × 2.5 m long × 1.7 m high, weight ∼10 tonne) consists of an eight-layer octagonal assembly of quarter-scale model bricks and model keys confined by a rigid aluminium restraint structure. The MLA model array has 20 bricks across its maximum cardinal direction, modelling 10 rings of the AGR core (Figure 2).

The array is enclosed by a rigid support frame and confined at the bottom by a rigid arrangement of plastic plates that mimic the required radial rocking features and in which the bottom component of each vertical column is mounted (Figure 3).

All of the AGR core component types are represented in the MLA, that is, fuel (lattice), interstitial, and filler bricks; filler, spacer, and loose bearing keys. The bottom face of each lattice brick has four rectangular protrusions called axial keys that locate in the axial keyways of an underlying brick. One of the two upper face diameters of the lattice brick

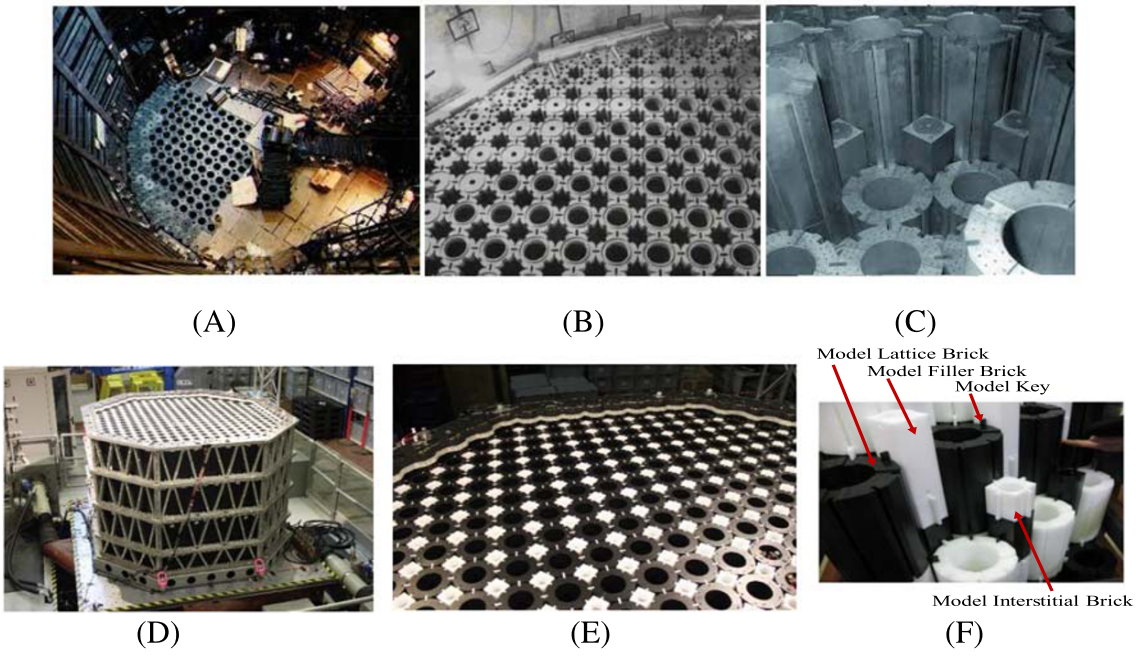

FIGURE 2 (A) and (B) advanced gas-cooled reactor (AGR) graphite core general view, during construction; (C) AGR graphite core components (courtesy: EDF Energy). (D) The multilayer array (MLA) rig on the shaking table, (E) the MLA rig top layer, and (F) the MLA model components. [Colour figure can be viewed at wileyonlinelibrary.com]

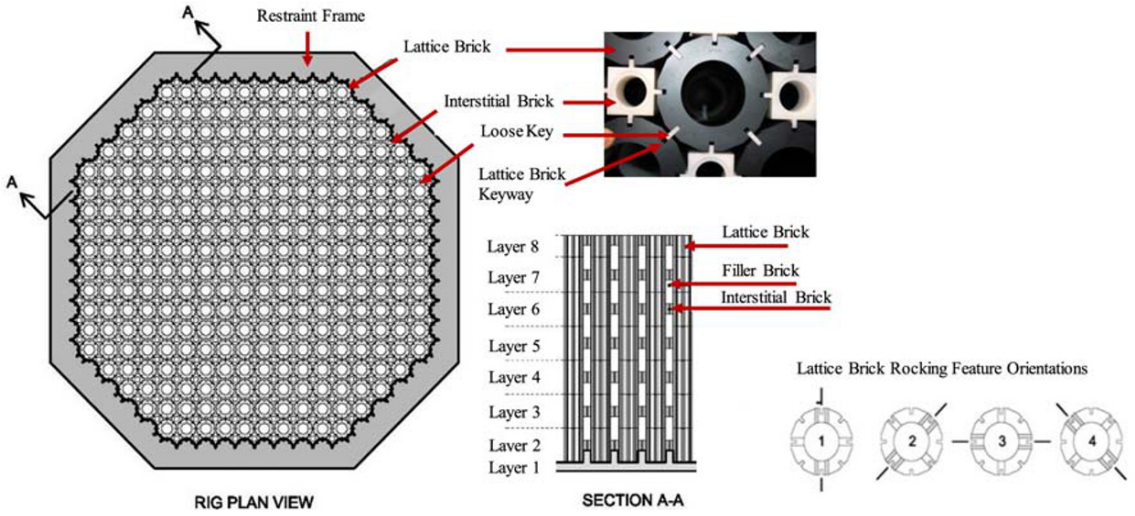

FIGURE 3 Plan view and cross-section of the multilayer array (MLA) model with rigid restraint frame. Base layer 1 is fixed while layers 2 to 8 are active [Colour figure can be viewed at wileyonlinelibrary.com]

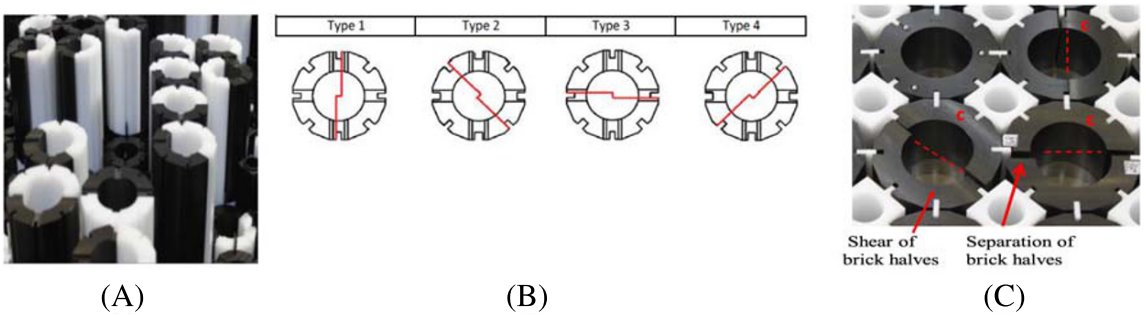

FIGURE 4 (A) Model cracked lattice bricks inside the array, (B) types of doubly cracked bricks with four crack orientations (shown in red), and (C) shearing and separation of brick halves (pictures taken during the multilayer array (MLA) building process, layers 4-7 cracked, and layer 8 intact) [Colour figure can be viewed at wileyonlinelibrary.com]

has a narrow flat ridge (a "rocking feature") on each side of the keyways that allows the upper brick to rock along a preferential direction. The rocking features are arranged in the core in four different orientations (Figure 3) so that all the lattice bricks can rock radially towards the centre of the array. The model bricks are stacked together in columns: the lattice bricks form the model fuel channels and the interstitial and filler bricks form the model control rod channels. All model array components are made of a rigid engineering plastic (acetal). More details on the MLA's design and mode of operation can be found in other studies.[5,6] The MLA incorporates the increased potential for brick displacements due to component degradation and the increased brick-to-brick clearances arising from late life shrinkage. The general dimensions of the model components are quarter-scaled from the prototype dimensions late in life (e.g., the brick-to-brick clearances between the model lattice bricks are 4 mm). In addition to the intact array components, the MLA can also include model doubly cracked lattice bricks that can be used in various percentages and orientations inside the array to model cores in an advanced state of degradation (Figure 4A,B). The cracking increases the potential for movement inside the array with possible implications on the keying system (i.e., increased potential of key-keyway disengagement due to shearing and separation of brick halves, see Figure 4C).

The rig is equipped with two vision systems for tracking top layer components, accelerometers in selected components, Hall effect sensors and linear potentiometers for brick-to-brick interface monitoring, and channel shape profile measurements, as well as Hall effect sensors for crack interface monitoring. The MLA rig yields the following outputs: relative and absolute displacements for selected array components, acceleration of selected array components, channel shape data and brick-to-brick interface data for selected channels, separation and shear between selected cracked brick halves, and position of selected keys in the keyways. With a total number of sensors exceeding 3,200, the MLA rig yields

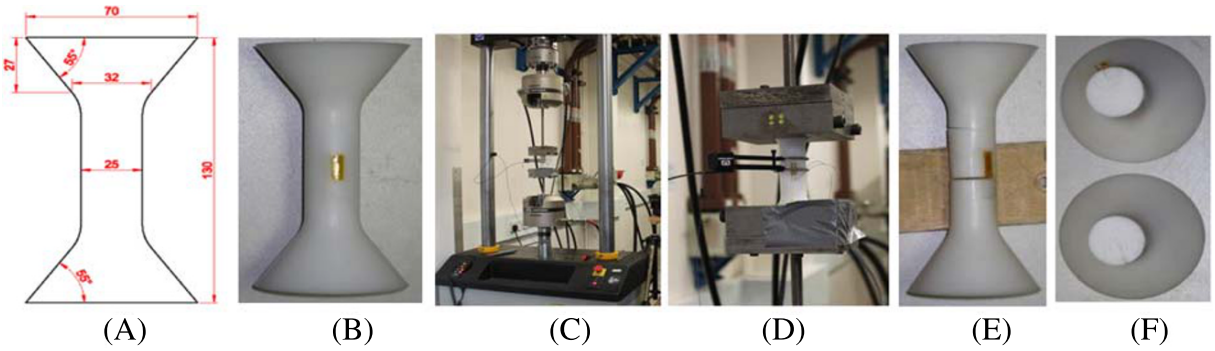

FIGURE 5 Tensile tests: (A and B) custom tensile test acetal specimen; (C) test setup within an axial test machine; (D) detailed view of a instrumented specimen and clamping arrangement; (E) characteristic failure mode, height of failure plane; and (F) failure plane section [Colour figure can be viewed at wileyonlinelibrary.com]

a large amount of data: approximately 1 TB of data (in ~400 seismic tests), for each tested configuration. This paper will focus only on array component displacement and channel shape data.

4 | MODEL MATERIAL AND MODEL COMPONENT CHARACTERISATION

4.1 | Material tests

During a seismic event, the AGR core would behave as an array of rigid bodies in which the relevant forces are the impact forces generated during the collisions between the components and the gravitational restoring forces. The impact forces depend on the local contact properties (i.e., contact stiffness and coefficient of restitution), hence a reasonable approximation for the ratio between the scaling factor for density and the scaling factor for stiffness between prototype and model had to be sought.[5] The engineering thermoplastic polyoxymethylene, known as acetal, was

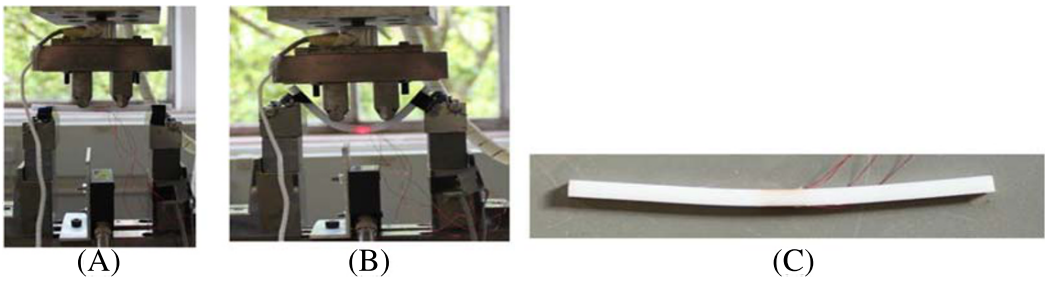

FIGURE 6 Flexural tests: (A) acetal specimen at beginning of test, (B) at maximum deflection, (C) characteristic failure mode [Colour figure can be viewed at wileyonlinelibrary.com]

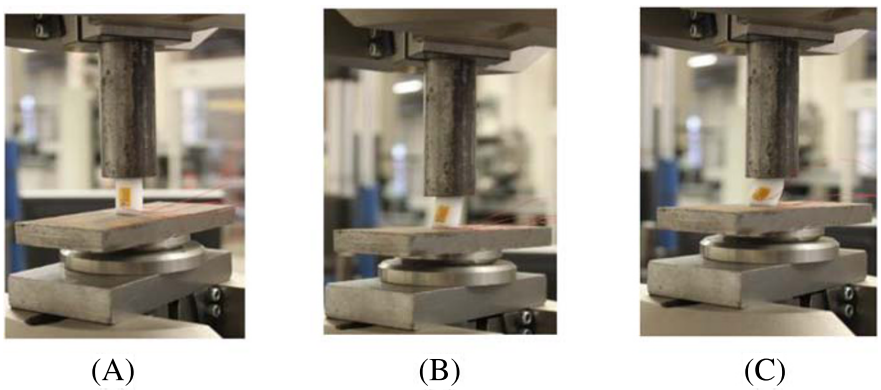

FIGURE 7 Compressive tests: (A) test setup with acetal specimen, (B) characteristic failure mode beyond yield, and (C) at ultimate failure [Colour figure can be viewed at wileyonlinelibrary.com]

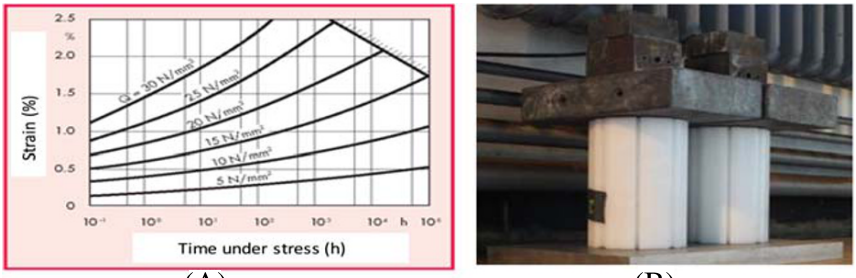

(A) (B)

FIGURE 8 Creep tests: (A) creep characteristics of acetal (Ticona Celanese Technical Sheet[8]) and (B) overview of the creep test setup for model lattice bricks [Colour figure can be viewed at wileyonlinelibrary.com]

selected for manufacturing the components of the MLA rig due to its reasonable density/stiffness ratio and durability (Ensinger Technical Sheet[7]). The following material properties were measured at UOB: tensile strength (Figure 5), bending strength (Figure 6), compression strength (Figure 7), creep (Figure 8), and friction (Section 4.2). The model material tests were carried out in accordance with ASTM D790–71 "Standard Test Method for Flexural Properties of Plastics and Electrical Insulating Materials" and ASTM D695–69 "Standard Test Method for Compressive Properties of Rigid Plastics." The creep characteristics of acetal are readily available from manufactures (i.e., such as Ticona Celanese Technical Sheet for Hostaform™[8]), see Figure 8A. The stress arising at the end face of the model fuel bricks due to gravity is conservatively estimated to be in the range 0.5 to 1.0 N/mm^2. From the lowest time-strain curve in Figure 8A, for 5 N/mm^2, we can estimate that the creep induced strain will be less than 0.4% over a year period. A creep of this order of magnitude should not change the shape of the model brick end features significantly. To verify that this was the case, the geometry of the end-face rocking features of a pair of fuel bricks were accurately measured, and then the bricks were loaded with a mass of 32 kg, twice the mass expected at the bottom layer of the array, and left for 3 months ($\sim 3 \times 10^3$ h), see Figure 8B.

At the end of this loading period, the geometry of the end-face rocking features of the tested pair of model fuel bricks was measured. The measurements instruments used were a digital vernier calliper, having a resolution of 0.01 mm, and a set of slip gauges having a resolution of 0.005 mm. A comparison of the measurements prior to loading and postloading revealed no significant change, with the maximum difference observed being 1 to 2 times the instrument's resolution which was within the measurement error. A visual examination of the rocking features revealed no observable difference post and prior to loading. Finally, a functional test was conducted by comparing the rocking of the pair of tested bricks to untested bricks. No distinguishable difference in rocking was observed. The tensile, flexural, and compressive tests were each carried out for six samples. A summary of the material test results supplied to the numerical modellers is given in Table 1.

4.2 | Friction analysis

In order to define what value for the friction coefficient is acceptable to supply to the numerical modellers, UOB embarked on a combined experimental and theoretical study targeting the fundamental behaviour of the individual array components where friction operates. A set of simple shaking table tests were conducted on reduced size arrays

TABLE 1 Material test results

Property	Mean	Deviation
Young's Modulus (GPa) (tensile tests results)	2.75	+0.03/−0.03
Tensile strength (MPa)	66.91	+0.08/−0.08
Young's Modulus (GPa) (flexural tests results)	2.91	+0.03/−0
Shore D hardness	89.12	+0.05/−0.05
Friction: static (measured)	0.35	0.018 (standard deviation)
Friction: dynamic (reported in Figure 12)	0.25	N/A
Creep induced strain: less than 0.4% over a 1 year.		

Note. Each type of test was carried out on six samples. Friction values discussed in Section 4.2.

and on individual components. The analysis investigated static and dynamic friction and their effect on component/array behaviour.

4.2.1 | Brick-on-base friction tests

Prior to the brick-on-base friction tests, the rocking potential during sliding was investigated. A 3 × 3 × 1 reduced height lattice brick SLA was built and tested in two configurations, at 4-mm pitch with and without loose bearing keys (Figure 9A). The base material used was duraluminium, having considerable higher friction than an acetal base, producing an overestimate of the rocking potential since higher friction leads to higher forces and an increased potential for rocking behaviour. Since they are much more likely to rock due to their unfavourable width-to-height aspect ratio, only the interstitial bricks were monitored with microelectromechanical systems (MEMS) accelerometers. No measurable rocking was observed for either of the two 3 × 3 × 1 array configurations tested.

The worst-case scenario from a rocking point of view is arguably an interstitial brick on its own since there are no restraints from the lattice brick keeping it from rocking. Therefore, tests were carried out on individual interstitial bricks sliding unaffected by other components, see Figure 9B,C. This configuration was tested on the shaking table for potential rocking over a range of excitation frequencies (3-6 Hz) and amplitudes (0.15-2.5 g). As expected, no slippage (sliding) was observed at lower excitation amplitudes. To verify that rocking did not occur, the root mean square (RMS) of both bricks' vertical response acceleration was calculated at steady state and compared with the PGA of the input motion (Figure 9C). For both interstitial bricks, there was no significant trend towards increased vertical response as the input motion increased to 2.5 g and the brick started sliding. However, three outliers to the general trend were observed for the black interstitial brick. These greater than expected responses were due to the brick hitting the rigid boundary for the 0.70, 0.85, and 1.00 g PGA input motions. This evidence, as well as visual observations, confirms that the interstitial bricks did not exhibit rocking during sliding at observable/measurable levels. The input acceleration and the horizontal response acceleration of one of the interstitial bricks shown in Figure 9B were plotted together on diagrams (Figure 10) showing the ramp up (transient) state and the steady-state response of the brick relative to the input motion for a range of input motion amplitudes.

At small input motions, 0.20 g PGA and smaller, a stick state exists and the brick moves with the motion of the shaking table. At large input motions, above 0.5 g PGA, the brick responds with slip behaviour, isolating itself from the large motions of the shaking table. At intermediate levels, the block responds with stick-slip behaviour, where the brick slides over a part of the forcing cycles and sticks over the rest. The stick-slip behaviour can be clearly observed for 0.25 and 0.30 g input amplitude. The sliding (the level of the plateau in the time histories) acceleration observed is between 0.20 and 0.25 g giving a dynamic coefficient of friction μ in the range 0.20 to 0.25.

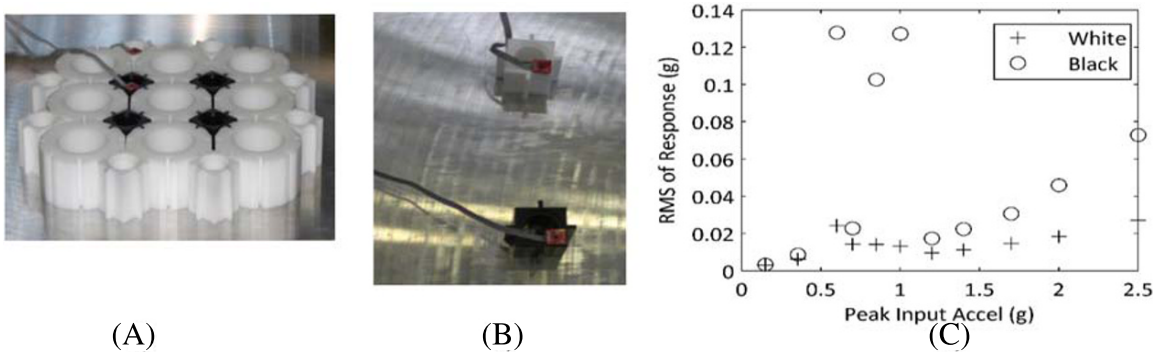

FIGURE 9 (A) Single-layer array 3 × 3 × 1 (L × W × H: 400 mm × 400 mm × 64 mm) with two interstitial bricks equipped with microelectromechanical systems (MEMS) accelerometers; (B) two individual interstitial bricks (white and black, L × W × H: 47 mm × 47 mm × 64 mm) with MEMS accelerometers; and (C) the root mean square (RMS) of vertical response acceleration for various input acceleration values [Colour figure can be viewed at wileyonlinelibrary.com]

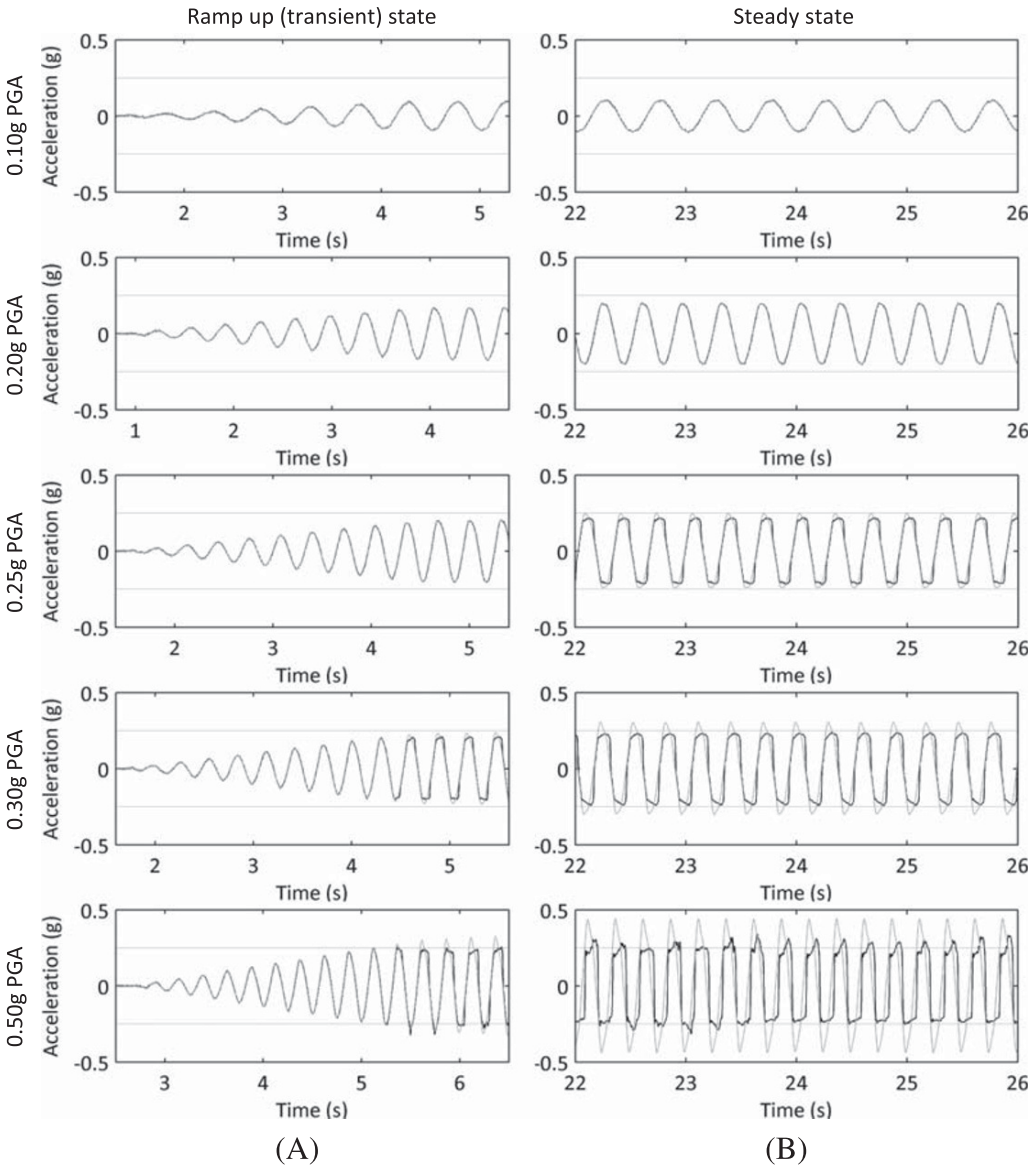

FIGURE 10 Sliding test results: (A) response horizontal acceleration at selected excitation amplitudes during ramp up (transient) stage and (B) during steady state. Input (black) and response (grey)

4.2.2 | Static friction tests

Static friction tests were carried out on an acetal disc (diameter: 70 mm; thickness: 9 mm) (Figure 11A) sliding on an acetal base. A model fuel brick adaptor with a 117-mm outer diameter, 65-mm inner diameter, and 2-mm thickness

FIGURE 11 (A) Acetal disc and (B) model lattice brick base on acetal base ready for friction testing [Colour figure can be viewed at wileyonlinelibrary.com]

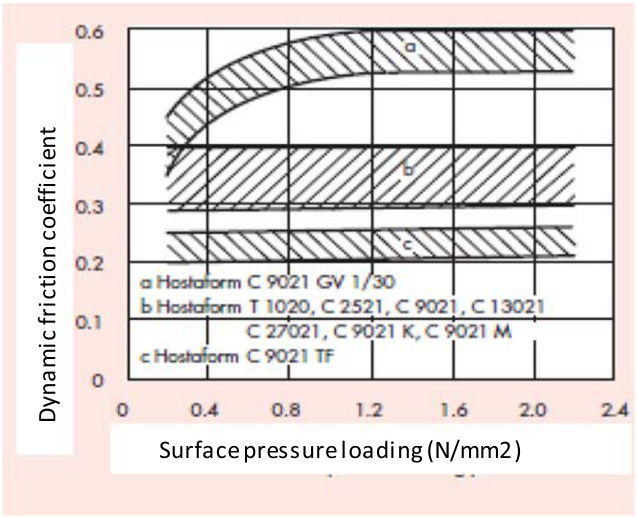

FIGURE 12 Dynamic friction coefficient vs. surface pressure loading for acetal (Hostaform C 9021TF marked as "c" in the diagram) (Ticona Celanese Technical Sheet[8]) [Colour figure can be viewed at wileyonlinelibrary.com]

TABLE 2 Static friction coefficients for selected pairs of materials

No.	Material 1	Material 2	μ_{static}
1	Acetal	Acetal	~0.35[a]
2	Graphite (temp. 20°C)	Graphite (temp. 20°C)	~0.10[b]
3	Graphite (temp. 350°C)	Graphite (temp. 350°C)	~0.20[b]

[a]Measured value.
[b]According to Driesner and Wagner.[9]

(Figure 11B) was also tested in order to check whether the contact area between the sliding surfaces affects the coefficient of static friction. The disc and the model lattice brick base were connected to an aluminium alloy hanger of known weight (45.24 g) by a light piece of string. Washers were added to the hanger incrementally and the total hanger weight corresponding to the inception of sliding was recorded. A minimum of 12 measurements were taken for each test configuration (a and b).

The measured static coefficient of friction was found not to vary with the contact surface area: both the acetal disc and the acetal lattice brick base gave similar coefficients of friction against the acetal surface (μ_{static} ~0.35, 12 measurements, standard deviation: 0.018) (Table 2).

The friction tests shown in Figure 11 investigated the static friction coefficient. It is important to note that in the MLA rig case, it is also the dynamic friction that requires scrutiny (Figure 12) as the components velocities in the physical rig may typically range between 0 and 1 m/s. In general, the dynamic coefficient of friction is influenced by the surface pressure loading, the sliding speed, the surface finish, and the ratio between the hardness values of the materials in contact. In our application, the pressure loading on the acetal components is much less than 0.4 N/mm^2 (for example, the pressure on the lowest interface of a lattice (fuel) column is ~0.03 N/mm^2). Figure 12 shows the dynamic friction coefficient for various grades of acetal (Ticona Celanese Technical Sheet). An average value of 0.25 is shown for the dynamic friction coefficient of Hostaform C 9021TF, which is the trade name of acetal, as given by Ticona Celanese GmbH. It is observed that the friction coefficient is stable for a pressure loading range of 0 to 2 N/mm^2. Following the above experimental tests, it was agreed that the following friction values were to be employed in the numerical work: brick-to-brick, $\mu_{static} = 0.35$, and $\mu_{dynamic} = 0.25$.

5 | NUMERICAL MODELLING

5.1 | Modelling approaches

Whole core numerical models of the AGR reactor exist in several different forms and software. There are models with 3D components using the NSCD software SOLFEC,[10] and stick-and-spring models using various finite element software

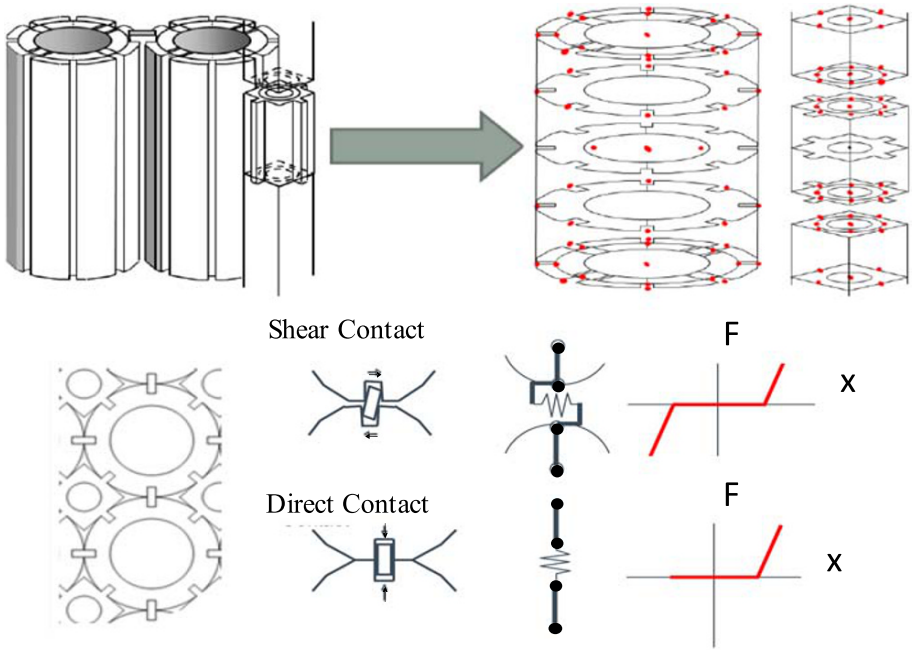

FIGURE 13 Representation of contacts in GCORE via nonlinear springs and dampers[12] [Colour figure can be viewed at wileyonlinelibrary.com]

(Parmec (https://parmes.org/parmec/), ABAQUS, Code_Aster,[11] and LS_DYNA). Currently, these models and software have different degrees of maturity and have the potential to complement one another in meeting particular requirements of simulation. A comparison between the MLA rig data and GCORE (an LS-DYNA nonlinear finite element model developed by ATKINS Nuclear[12] was presented in a previous publication.[6] Under seismic excitation, the MLA behaves as an array of rigid bodies in which the relevant forces are the impact forces generated during the collisions between the components and the gravitational restoring forces. In GCORE (a "stick-and-spring" model), the core components are represented as rigid bodies and the contacts between them are represented using nonlinear spring/damper pairs connected to nodes (Figure 13).

The energy restitution after a brick-to-brick collision depends heavily on the actual layout of components in a zone of investigation (i.e., presence or absence of keys, cracked bricks, and locking of keys/bricks). However, friction forces will also exist between the sliding surfaces of the array components and such forces may affect the mechanics of the keying systems. In order to capture such forces in the numerical models, a reasonable representation of viscous friction and Coulomb friction had to be sought. The older versions of GCORE modelled friction solely via viscous damping, while the current version of GCORE in ABAQUS includes a representation of the Coulomb kinetic friction law,[13] which leads to reasonable predictions of core behaviour that compare well with the MLA rig results.[6] This current GCORE model approximates the friction force as follows (Figure 14):

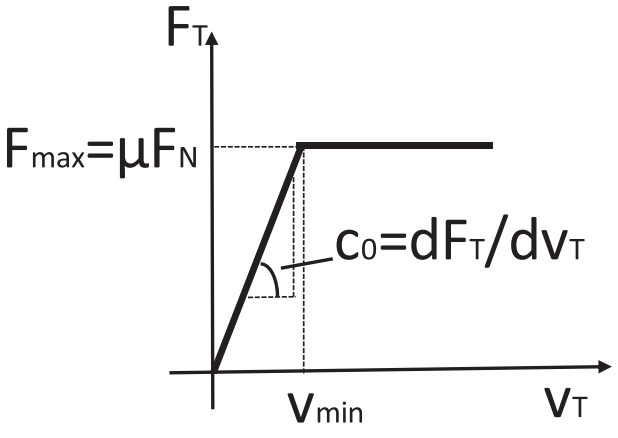

FIGURE 14 Force-velocity curve for friction representation in GCORE: F_N and F_T are the normal and the tangential components of contact force, C_0 is the damping coefficient, and μ is the friction coefficient

- At low velocities: friction force (F_T) is the friction damping force (proportional to the relative velocity (v) of the contacting bodies).
- At higher velocity: friction force (F_T) is the Coulomb friction, calculated as the elastic reaction force (F_N) normal to the plane in which friction acts multiplied by the friction coefficient (μ).

Figure 14 shows that at zero velocity, the friction force is zero, hence the model cannot implement static friction. This was designed to avoid instabilities in the model, arising from the existence of friction in the absence of any other applied force (i.e., friction force alone would cause an artificial acceleration of the body). A suitably large damping coefficient (C_0) is recommended in the model such that the full friction force is reached at very low velocities.

It is important to note that viscous damping and Coulomb friction operate differently over the forcing cycle. Their modes of operation are discussed in more detail in the following section.

5.2 | Theoretical considerations on friction

The characteristics of Coulomb friction damping and viscous damping are, in many ways, very different. On one hand, Coulomb friction damping dissipates energy evenly during the slippage phase (starting when inertia force is equal to the friction force) of the forcing cycle. On the other hand, the viscous damping energy dissipation ranges from none at peak inertia force to maximum at the inertia force reversal point (zero inertia force), that is, directly proportional to the brick's velocity. In this section, the two damping mechanisms will be compared and, for a special case, a relationship between them will be derived. From purely theoretical point of view, it is possible to produce a relationship between viscous and Coulomb friction damping by assuming that the energy dissipated through either damping mechanisms is the same over a forcing cycle for harmonic excitation. A conventional viscously damped single-DOF oscillator with a mass m, stiffness k, and damping c, excited through base acceleration has the following equation of motion:

$$m\ddot{x} + c\dot{x} + kx = m\ddot{x}_g, \tag{1}$$

where *dot* denotes differentiation with respect to time. By dividing through 1 with the mass m, it produces the following expression:

$$\ddot{x} + \frac{c}{m}\dot{x} + \frac{k}{m}x = \ddot{x}_g. \tag{2}$$

Now, by introducing a new damping parameter C and employing the relationship between the system's mass m, stiffness k and natural frequency ω_n

$$\omega_n = \sqrt{\frac{k}{m}}, C = \frac{c}{m}, \tag{3}$$

the system's equation of motion can be further simplified as follows:

$$\ddot{x} + C\dot{x} + \omega_n^2 x = \ddot{x}_g. \tag{4}$$

The energy per unit mass dissipated through viscous damping for this system is

$$E_{d_v} = \int C\dot{x}dx = \int_0^t C\dot{x}^2 dt. \tag{5}$$

For the Coulomb friction-damped case, the equation of motion of a friction damped single-DOF oscillator with a mass m, stiffness k, and friction coefficient μ, excited through base acceleration $\ddot{x}_g$, can be expressed in the following form:

$$m\ddot{x} + \mu mg + kx = m\ddot{x}_g, \tag{6}$$

where g is the gravitational acceleration (9.81 m/s^2). In the same manner as before, the equation of motion is simplified by dividing by the mass m on both sides and applying the relationship between the system's mass m, stiffness k, and natural frequency ω_n 3, 6, to produce the following expression:

$$\ddot{x} + \mu g + \omega_n^2 x = \ddot{x}_g. \tag{7}$$

The energy per unit mass dissipated through Coulomb friction damping for this system is as follows:

$$E_{d_f} = \int \mu g dx. \tag{8}$$

Now, assume that the input motion is harmonic and the system's response at steady state takes the simplest possible form

$$x = \chi \sin(\omega t - \phi), \tag{9}$$

where χ is the steady-state response amplitude, ω is the forcing frequency, and ϕ is the phase angle.

By making the energy per unit mass dissipated through viscous damping 5 and through Coulomb friction damping 8 the same over one cycle, a relationship between the viscous damping and Coulomb friction damping can be defined. First, 9 is differentiated and substituted into the viscous damping energy expression 5, producing the following expression for the energy dissipated through viscous damping:

$$E_{d_v} = \int_0^t C\dot{x}^2 dt = C\omega^2\chi^2 \int_0^{2\pi/\omega} \cos^2(\omega t - \phi) dt = C\pi\omega\chi^2. \tag{10}$$

By applying the response amplitude as the limits to 8 and multiplying by 2 to account for each halve of the forcing cycle, an expression for the energy per unit mass dissipated through Coulomb friction damping over one forcing cycle is produced,

$$E_{d_f} = 2\int_{-\chi}^{\chi} \mu g dx = 4\mu g\chi. \tag{11}$$

Finally, the energy per unit mass dissipated through viscous damping 10 is made equal to the energy per unit mass dissipated through Coulomb friction damping 11, leading to the following expression:

$$C = \frac{4\mu g}{\pi\omega\chi}, \tag{12}$$

assuming the steady-state response χ is the same in both cases. Now, for mass proportional Rayleigh damping, the coefficient C can be represented as

$$C = \frac{c}{m} = \frac{2\zeta\omega_d m}{m} = 2\zeta\omega_d. \tag{13}$$

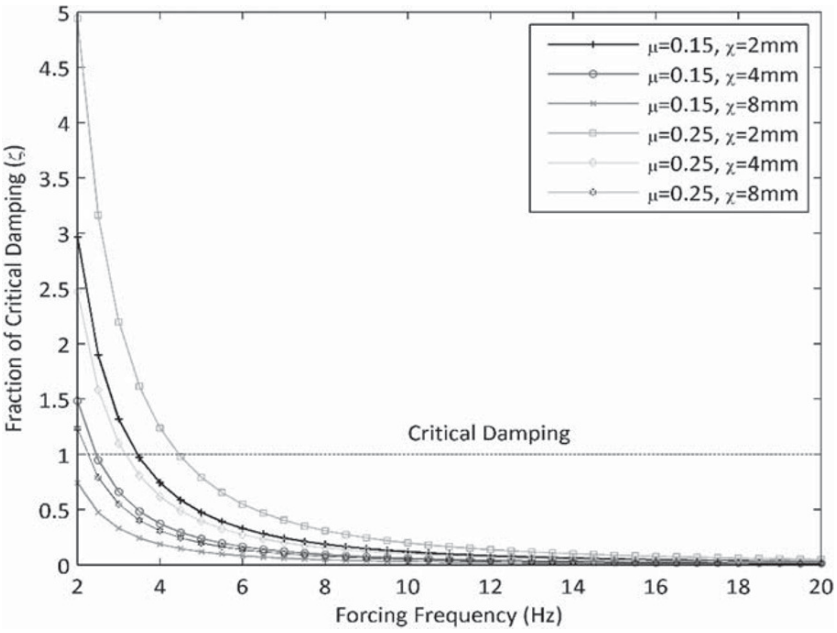

FIGURE 15 Damping ratio ζ versus forcing frequency for selected frictional coefficients μ and response amplitudes χ

By substituting 13 into 12 and assuming the frequency to be damped ω_d is the same as the forcing frequency ω, the following expression for the viscous damping ratio ζ as a function of the friction coefficient μ, the forcing frequency, ω and the response displacement amplitude χ, can be produced:

$$2\zeta\omega = \frac{4\mu g}{\pi\omega\chi} \Rightarrow \zeta = \frac{2\mu g}{\pi\omega^2\chi}. \tag{14}$$

To get a feeling of how the control variables, that is, the friction coefficient μ, the forcing frequency ω, and the response displacement amplitude χ, influence the amount of equivalent viscous damping, the equivalent viscous damping ratio ζ (equation 14) was plotted as a function of the forcing frequency ω for a range of practical values for the friction coefficient μ and the response displacement amplitude χ, see Figure 15.

Although it is possible to produce an expression relating the equivalent viscous damping to the friction properties of a Coulomb friction-damped system, it is apparent from the expression itself that achieving similitude between those two damping mechanisms throughout the system's response space is impossible. For the special case when the Rayleigh damping frequency is the same as the forcing frequency and the steady-state response amplitudes are the same for both types of damping, the equivalent viscous damping ratio ζ versus the forcing frequency is presented for practical values of the friction coefficient μ and the response displacement amplitude χ. For this case, a very wide range of equivalent viscous damping ratios are observed, ranging from underdamped to massive overdamping. A better outcome could be achieved by allowing the Rayleigh damping frequency and the forcing frequency to be different or by assuming a difference in the response amplitudes. This section has highlighted the differences between Coulomb friction damping, existing between the bricks in the MLA, and viscous damping employed in some older numerical models (old versions of GCORE for example). It is important to note that, currently, there are computational models that include Coulomb friction (GCORE's latest version and SOLFEC).

5.3 | SOLFEC

The unprecedented complexity of the MLA core model is due to its large number of components (~44,500) and contacts, which can feature millions of DOFs during a seismic event. SOLFEC[10] attempts to address such complex systems through the use of a novel contact formulation based on the NSCD method by Moreau[14] and Jean.[15] The

NSCD method involves the use of dynamics' equations, nonsmooth modelling of unilateral contact, Coulomb's law, and fully implicit algorithms. SOLFEC includes a 3D representation of the geometry of the components being studied, and it does not make use of repulsive springs to prevent interpenetration of the bodies. It is worth noting that the GCORE approach on the other hand does not permit arbitrary contacts between bodies as appropriate spring/damper pairs must be predefined at predefined locations (nodes) as part of the model. While GCORE is relatively simple computationally, it limits the range of behaviour which can be captured: for example, it cannot simulate situations where a key can disengage from its keyway. SOLFEC, being a solid-body code, allows any contacts to be detected and resolved (Figure 16). The SOLFEC model's ability to simulate and study key disengagement and postdisengagement behaviour in the core becomes more important as clearances in the core increase over time due to irradiation-driven shrinkage of the graphite bricks and keys. Moreover, SOLFEC enables simulation of deformable bodies with any type of cracks present in the components. This is a convenient way to accurately represent the deformation of the whole core models that include various layouts and percentages of cracked bricks.

SOLFEC models friction by Coulomb's law application for each unilateral contact between the moving bodies and by the Signorini condition that prevents body overlapping.[10] SOLFEC essentially models the contact between two bodies as a constraint on their relative velocity, with the most obvious form of this constraint being that there is zero relative velocity between the contacting points (Figure 17).

It is important to observe that static friction is represented in the model. Crucially, the NSCD method permits an implicit solution rather than an explicit solution as is normally used for such dynamic problems. As such, much larger time steps are stable, which may allow the simulation to be much faster overall.

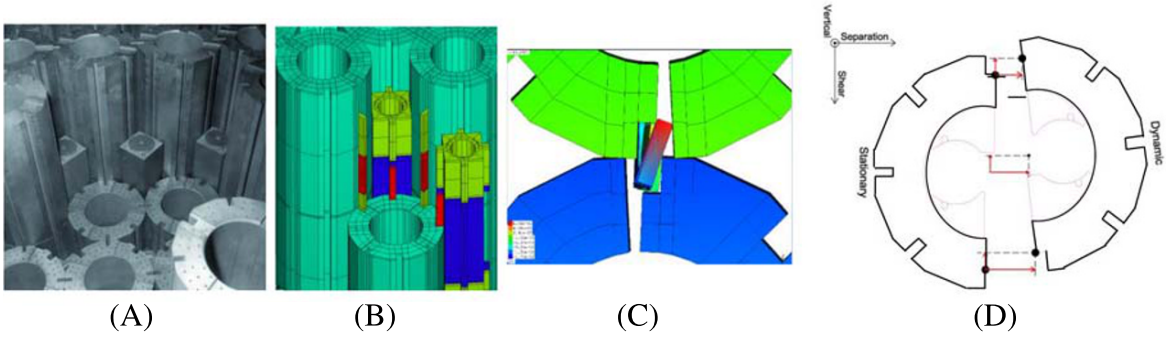

FIGURE 16 Modelling in SOLFEC (A, physical model; B, SOLFEC model [cross section]; C, SOLFEC model [key-keyway contact modelling for two adjacent cracked lattice bricks]; D, shear and separation of doubly cracked brick halves) [Colour figure can be viewed at wileyonlinelibrary.com]

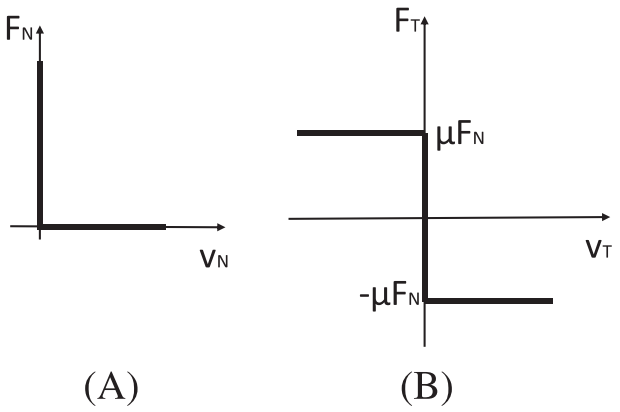

FIGURE 17 The (A) Signorini–(B) Coulomb frictional contact law employed in SOLFEC (F_N, F_T, v_N, and v_T are the normal and the tangential components of contact force and relative velocity and μ is the coefficient of friction)[10]

6 | MLA PHYSICAL MODEL: SOLFEC RESULTS COMPARISON

The model material and model component characterisation work described in Section 4 supplied the set of material parameters that were trialled in the numerical model. SOLFEC numerical simulations and MLA rig tests were run in parallel to test the modelling assumptions and to assess the model's capability for predicting the dynamic response. A discussion of this comparative study is presented in the following sections.

6.1 | Sensitivity studies

6.1.1 | Friction sensitivity analysis

Both the material manufacturer's dynamic coefficient of friction (0.25) and the UOB measured static coefficient of friction (0.35) were trialled in the numerical model. An example is presented for the MLA rig test T2432 for which the HRA input displacement and the acceleration time histories are shown in Figure 18B. The test was conducted on an MLA array with 50% cracked bricks in layers 4 to 7, and the HRA seismic input was applied in the 45° direction (see axis convention in Figure 18A).

Figure 19 compares the MLA top layer X and Y displacements relative to the rig frame for the instrumented lattice bricks in the top layer. Reducing the friction coefficient from 0.35 (Figure 19A,B) to 0.25 (Figure 19C,D) increases the range in displacement experienced by the top layer array components, although the increase is not particularly significant (0.4 mm in X, 0.6 mm in Y), suggesting that SOLFEC's prediction of displacement ranges is not significantly sensitive to these friction coefficients. The SOLFEC results compare well with the rig data (Figure 19E,F) in pattern and magnitude. A comparison of the X and Y relative displacement of lattice brick LB2521 in the MLA top layer (layer 8) is presented in Figure 20. The numerical simulations do not appear to be significantly sensitive to the selection of friction coefficient, although the measured static coefficient of friction value of 0.35 appears to simulate behaviour most comparable with the test rig.

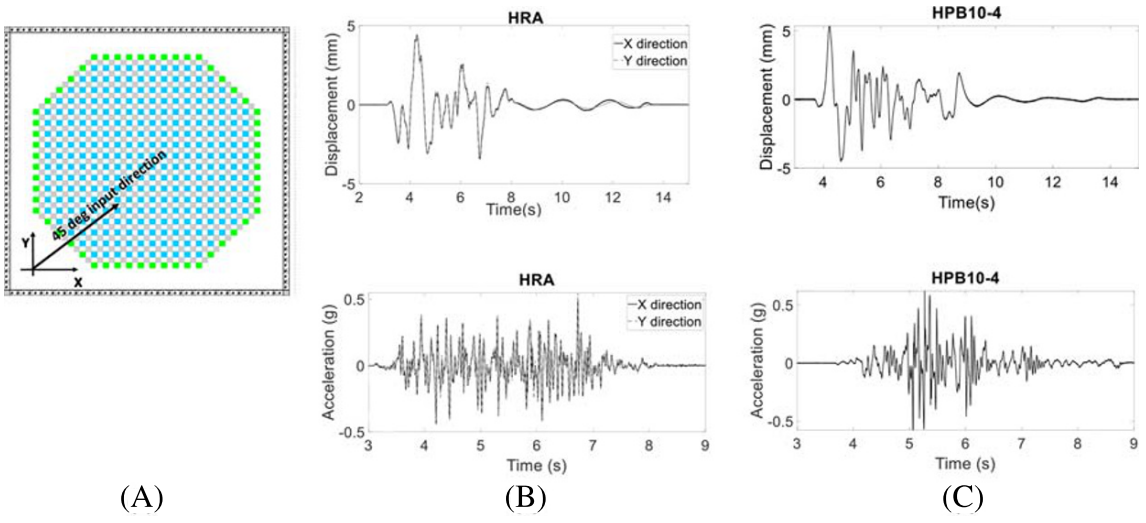

FIGURE 18 (A) Axis convention: multilayer array (MLA) reference system aligned with the shaking table reference system, (B) HRA input displacement and input acceleration in MLA test T2432 (50% cracked array, input applied in the 45° direction), and (C) HPB10^{-4} input displacement and input acceleration in MLA test T2349 (50% cracked array, input applied in the X direction) [Colour figure can be viewed at wileyonlinelibrary.com]

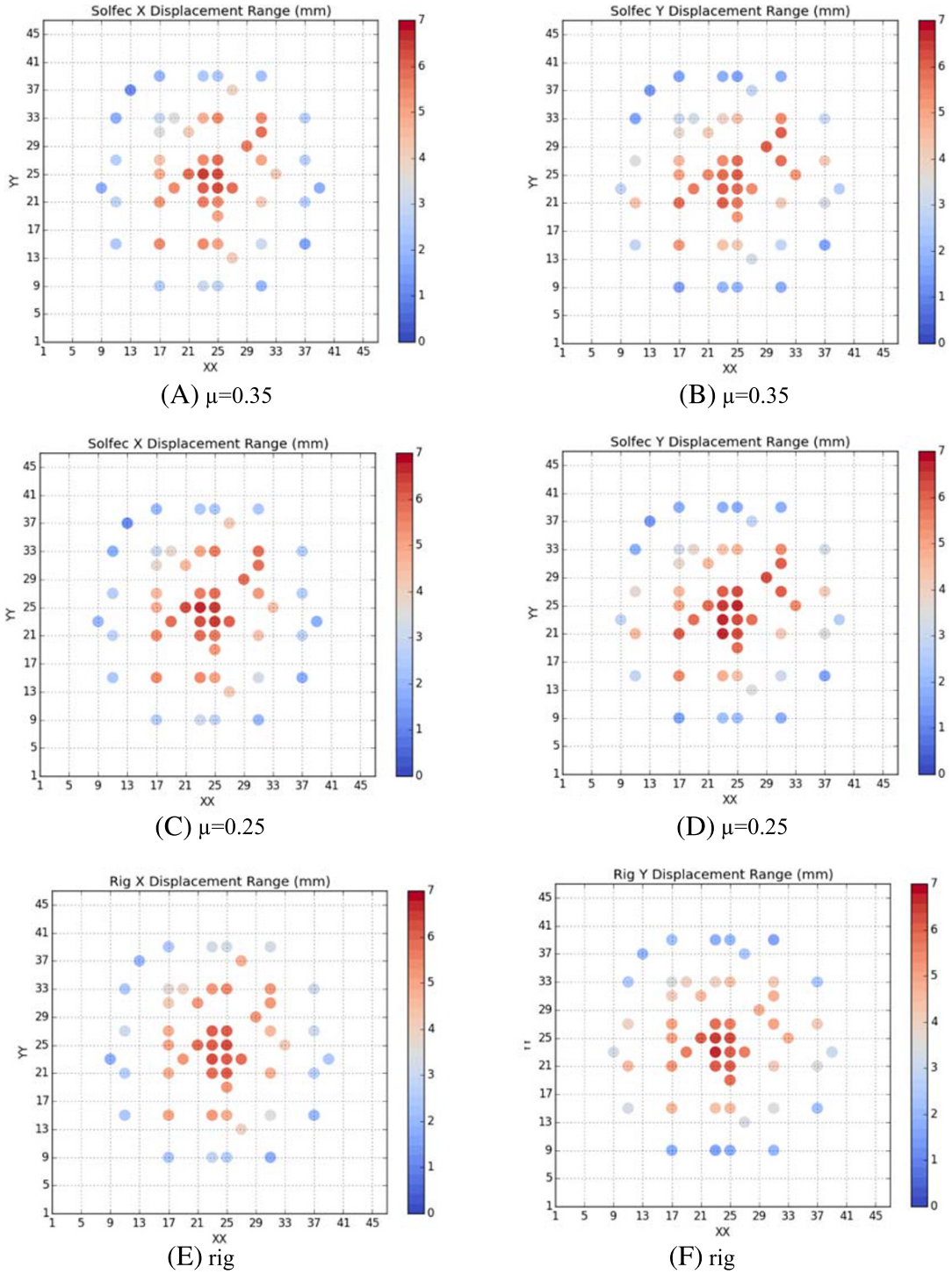

(A) μ=0.35 (B) μ=0.35

(C) μ=0.25 (D) μ=0.25

(E) rig (F) rig

FIGURE 19 Friction sensitivity analysis: X and Y relative displacement of selected instrumented bricks in the top layer, in test T2432, 50% cracked array, seismic input: HRA, 45° direction. (A), (B), (C), and (D) SOLFEC simulations and (E) and (F) multilayer array (MLA) rig results. (A) μ = 0.35, (B) μ = 0.35, (C) μ = 0.25, (D) μ = 0.25, (E) rig, and (F) rig [Colour figure can be viewed at wileyonlinelibrary.com]

6.1.2 | Time-step sensitivity analysis

The selection of an appropriate time step to use in the SOLFEC simulations was an important aspect of the code performance, as the MLA model is of considerable size and requires significant computational power. The average number of nodes per solid body is about 60 and each body has 3DOFs; hence, the number of DOFs in the model

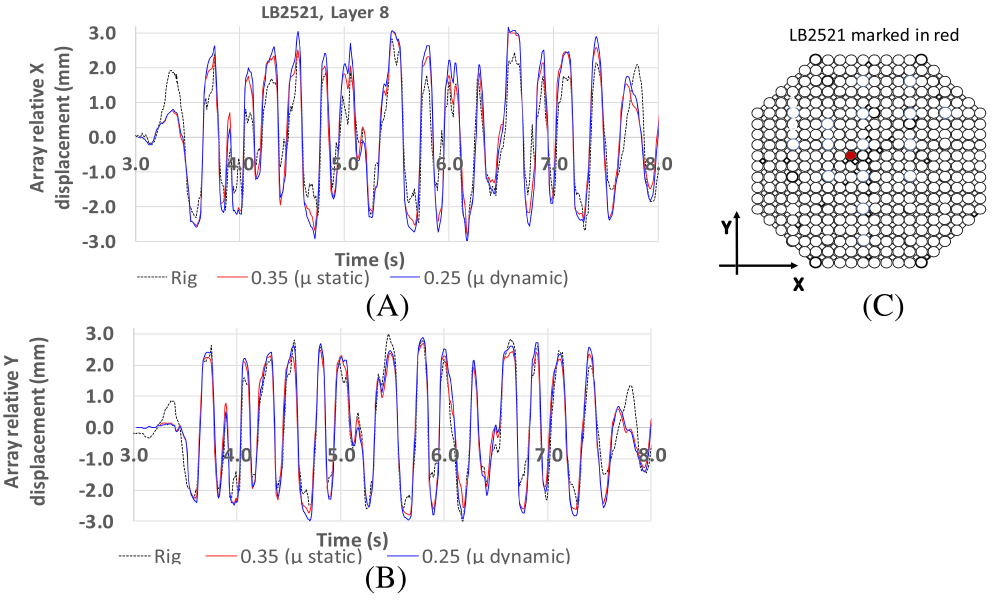

FIGURE 20 SOLFEC simulations for two friction coefficients and rig results: (A) relative displacement time history on X and (B) on Y of lattice brick LB2521 in the multilayer array (MLA) top layer (C), in test T2432, 50% cracked array, seismic input: HRA, 45° direction [Colour figure can be viewed at wileyonlinelibrary.com]

can go up to 44,500 * 3 * ~60 = 8,000,000. Increasing the number of processor cores the analysis was run on, proportional to the number of DoFs, did not result in a constant wall clock run time, largely due to the increase in the communication overhead as more cores were used. Preliminary investigations reviewing the analysis performance of MLA simulations indicated that there was little benefit in running simulations on more than 384 processor cores. Assuming an analysis duration of 8 s and a running environment of 384 cores, a typical MLA simulation took approximately 3 days to complete using a time step of 1×10^{-4}s and approximately 14 days to complete using a time step of 1×10^{-5}s. Figure 21 presents the relative displacement on (A) X direction and on (B) Y direction for lattice brick LB2521 in test T2432. The difference in results was not considered significant enough to justify the use of the much smaller 1×10^{-5}s time step. Hence, all the following SOLFEC MLA models reported have used a time step of 1×10^{-4}s.

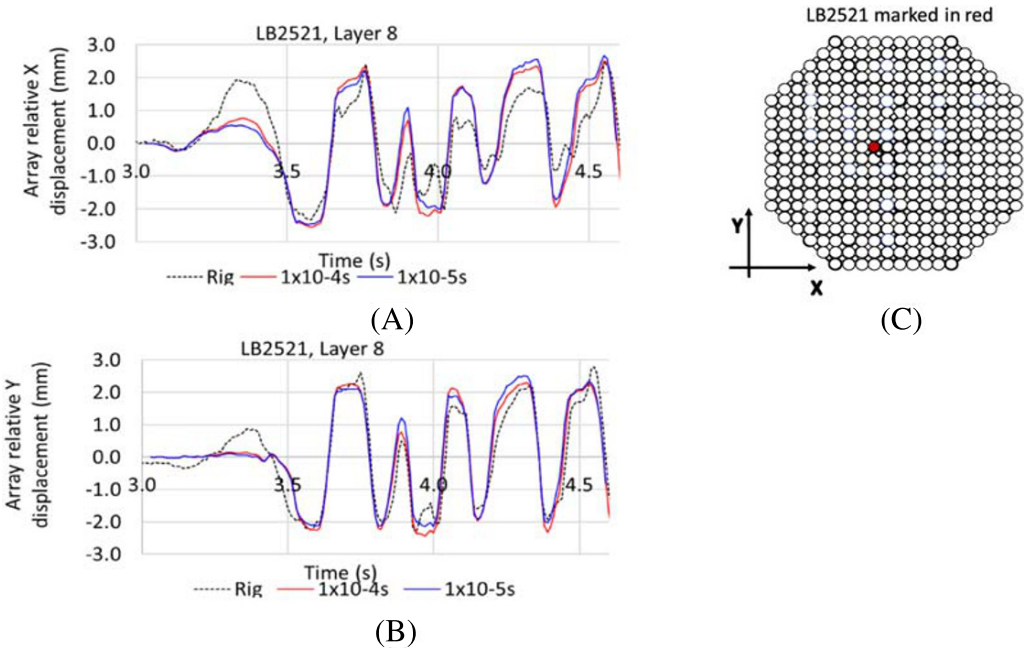

FIGURE 21 SOLFEC simulations for two simulation time step values and rig results: (A) relative displacement time history on X and (B) on Y of lattice brick LB2521 in the multilayer array (MLA) top layer (C), in test T2432, 50% cracked array, seismic input: HRA, 45° direction [Colour figure can be viewed at wileyonlinelibrary.com]

6.1.3 | Damping sensitivity analysis

A sensitivity analysis was carried out by simulating rig test T116 (Figure 22) in SOLFEC for two stiffness proportional damping coefficients (5×10^{-5} and 1×10^{-5}). A comparison of the relative displacement of lattice brick LB2521 in the top layer in the direction of the driving motion is shown. As expected, reducing the value of damping results in more energetic collisions and greater array displacements. The results suggest that whilst the simulation is not particularly sensitive to the reduction in damping parameter, the value of 5×10^{-5}, most appropriately predicts the peak displacements of LB2521. Lattice column distortions for the sensitivity analysis are also presented in Figure 23 for comparison against the rig test results for a damping value of 5×10^{-5}.

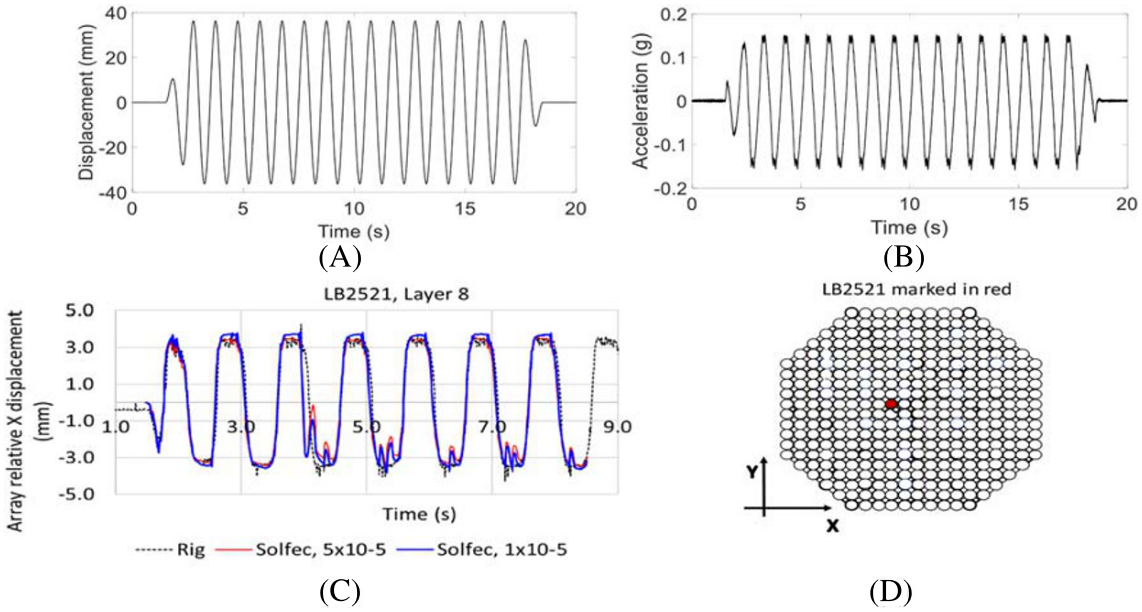

FIGURE 22 Damping sensitivity analysis: (A) sinusoidal input displacement and (B) input acceleration time history employed in test T116, intact array, input: 1 Hz frequency, 36 mm amplitude, X direction. (D) Relative X displacement of lattice brick LB2521 for rig and SOLFEC with two damping coefficients and (D) the multilayer array (MLA) top layer [Colour figure can be viewed at wileyonlinelibrary.com]

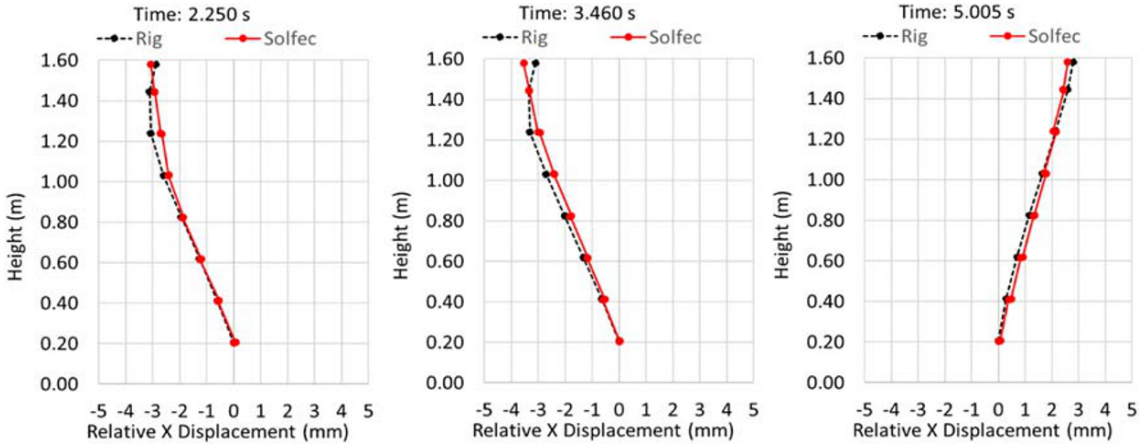

FIGURE 23 Column distortions of lattice brick column 2,521 at times of peak array relative displacements, in test T116, intact array, input: 1 Hz frequency, 36 mm amplitude, X direction, for damping value of 5×10^{-5} [Colour figure can be viewed at wileyonlinelibrary.com]

6.2 | Effect of cracking

Understanding the effect of introducing cracked lattice bricks in the array is a fundamental objective of this study. As cracking increases the mobility of the array, the risk of channel distortion during a seismic event increases. It is important to observe the response of the MLA for both intact and cracked arrays in both experiments and SOLFEC models. The cracked arrays included cracked bricks in layers 4 to 7, while the top layer (layer 8) was kept intact. Figure 24 presents a snapshot of lattice brick channel 2,521 at times of peak array relative X displacements, for an intact array, in test T116 (input described in Figure 22) and Figure 25 presents a snapshot of the same channel for a 50% cracked array in test T2349 (HPB10^{-4} seismic input presented in Figure 18C). The experimental outputs and the SOLFEC simulations for column distortions appear to be in good agreement, with maximum deviation of less than 0.5 mm between results. The distortion appears to be the largest in layers 6 and 7 (height 1.2-1.4 m), while the intact top layer has an anchoring effect on distortion (reduced potential of component movement in the uncracked layer 8).

The maps in Figure 26 present the maximum displacement (relative to the rig frame) for a set of instrumented lattice bricks in the top layer of the MLA, in test T2349 (50% cracked array in layers 4 to 7, HPB10^{-4} seismic input applied in X direction, peak acceleration 0.5 g). The relative displacements are the largest towards the centre of the array (up to ~9 mm), due to the brick-to-brick gap accumulation and the less pronounced influence of the rigid boundary. The top

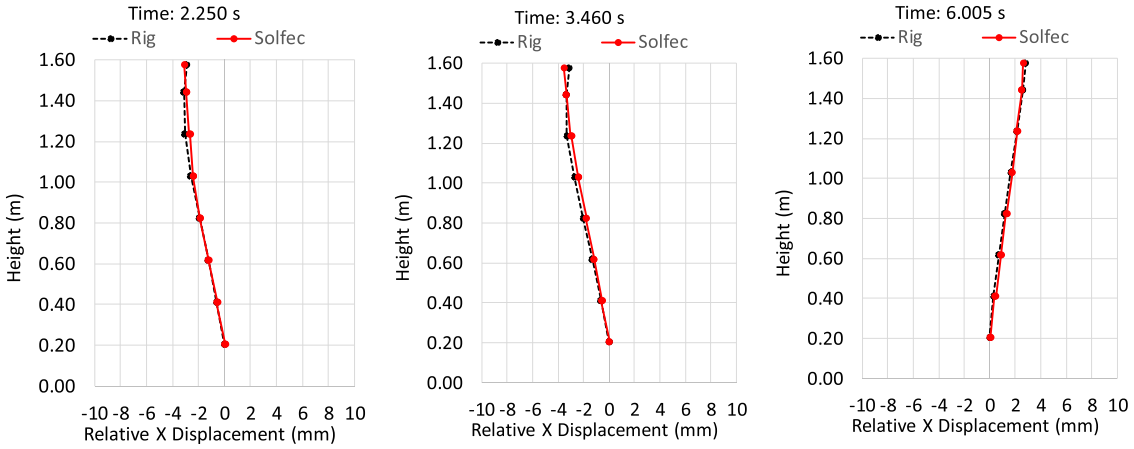

FIGURE 24 MLA1 (intact array), column distortions of lattice brick column 2,521 at times of peak array relative X displacements, in test T116, input: 1 Hz sinusoidal dwell, 36 mm target magnitude [Colour figure can be viewed at wileyonlinelibrary.com]

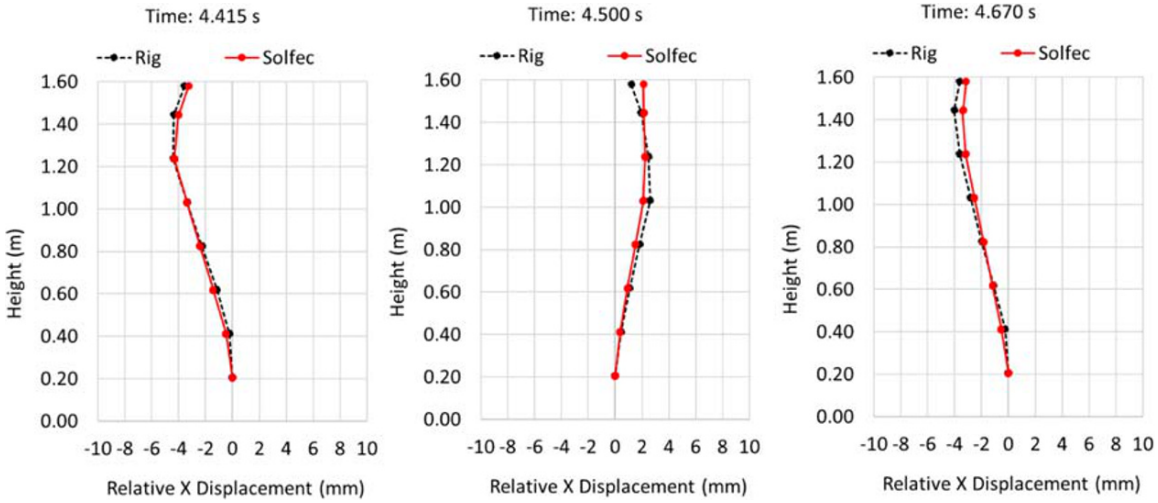

FIGURE 25 MLA4 (50% cracking). Column distortions of lattice brick column 2,521 at times of peak array relative X displacements, in test T2349, seismic input: HPB10^{-4}, X direction, peak acceleration 0.5 g [Colour figure can be viewed at wileyonlinelibrary.com]

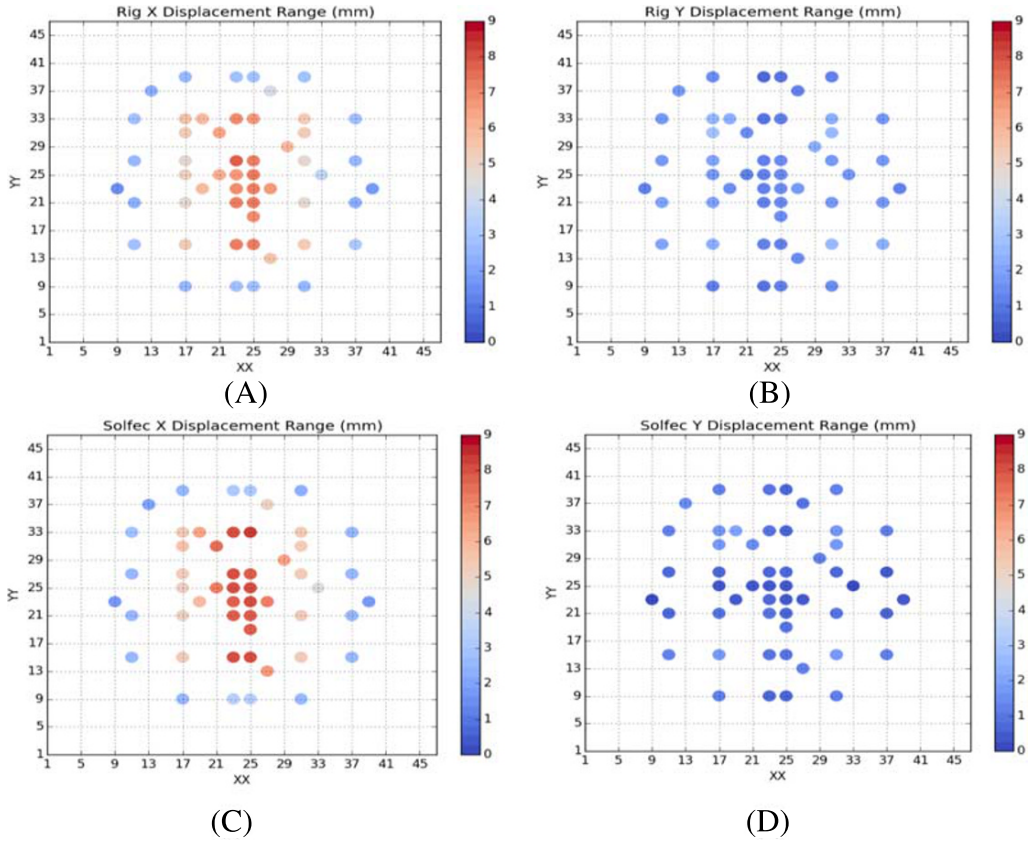

FIGURE 26 MLA4 (50% cracking). (A and C) Relative X displacement and (B and D) relative Y displacement of top layer lattice bricks, T2349, 50% cracked array, seismic input: HPB10^{-4}, X direction, peak acceleration 0.5 g, (A and B) rig maps and (C and D) SOLFEC simulation maps [Colour figure can be viewed at wileyonlinelibrary.com]

layer bricks moved more in the direction of input application (X in this case), while the Y relative displacements appear to be small (∼1-3 mm). The experimental outputs and the SOLFEC simulations (Figures 19-26) show similar patterns of response, with displacements of comparable values and larger displacements being measured/simulated in the central area of the array. Overall, the rig and the numerical code results are typically within 0.5 mm of each other, for both individual component displacements and channel distortions.

7 | CONCLUDING REMARKS

This paper features an important, yet unconventional, structural engineering project that provides experimental and numerical predictions to support the AGR seismic resilience assessments. The seismic resilience assessments are an important component of the AGR safety cases, hence the industrial and the societal impact of this work is very high. The physical model developed at UOB (the MLA rig) is a tool of high complexity, unique in the world, that models an AGR core at quarter scale. Its number of model components and measurement sensors are pushing the boundaries of design in instrumentation, data acquisition, and data processing. The rig can provide displacement and acceleration data for the array components, as well as channel profile measurements in seismic tests. In parallel, the numerical model developed in SOLFEC addresses the AGR core through the use of a novel NSCD formulation. SOLFEC is able to model a wide range of intact and cracked core scenarios, with the ability of simulating friction and of detecting array component position. The main objective of the project was to assess the shape of the model control rod/fuel rod channels during a seismic event for both intact and degraded model arrays (arrays containing model cracked bricks) in both the physical and the numerical model, as keeping the channels within their straightness tolerance is a fundamental requirement of the AGRs. The SOLFEC model's prediction of displacement ranges was found not to be overly sensitive to the damping coefficient. Reducing the friction coefficient increased the range of displacement experienced by the top

layer array components, although the increased range was not particularly significant. The SOLFEC results for channel shapes compared well with the MLA rig data in pattern and magnitude of displacement range, with a typical difference of less than 0.5 mm between the two. The distortion appears to be the largest in array layers 6 and 7, while the intact top layer has an anchoring effect on the array by limiting distortion. The relative displacements of the array components were found to be the largest towards the centre of the array, due to the brick-to-brick gap accumulation and the less pronounced influence of the rigid boundary. The direct comparison results show good agreement between the SOLFEC model and the MLA physical model in predicting component displacement and channel distortion, thus increasing the confidence in both tools. Both rig and code are versatile in terms of array component configuration and seismic input conditions, hence a variety of core scenarios can be tested that can explore in detail the AGR mechanics. The MLA-SOLFEC project supports the AGR safety cases, hence helps to deliver a safe and reliable electricity supply to the United Kingdom.

ACKNOWLEDGEMENTS

The authors would like to thank EDF Energy for financial and technical support. The views expressed in this paper are those of the authors and do not necessarily represent those of EDF Energy.

ORCID

Luiza Dihoru https://orcid.org/0000-0001-6971-195X
Adam J. Crewe https://orcid.org/0000-0002-0661-6346
Matt Dietz https://orcid.org/0000-0002-1914-1060

REFERENCES

1. National Audit Office, *The Department of Energy & Climate Change: Nuclear power in the UK*, 19, 13/07/ 2016.
2. Flewitt, Wickham (Eds). *Engineering Challenges Associated with the Life of Graphite Reactor Cores*. EMAS Publishing; 2015 ISBN-978-0-9576730-5-2.
3. Neighbour GB (Ed). *Modelling and Measuring Reactor Core Graphite Properties and Performance*. Cambridge: RSC Publishing; 2013 ISBN-978-1-84973-390-8.
4. Dihoru L, Crewe AJ, Taylor CA, Horgan T. In: Neighbour GB, ed. *Shaking Table Experimental Programme, Proc. of the Conference on Modelling and Measuring Reactor Core Graphite Properties and Performance*. Cambridge, UK: Aston University; 2011.
5. Dihoru L, Oddbjornsson O, Kloukinas P, et al. The development of a physical model of an advanced gas-cooled reactor core: outline of the feasibility study. *Nucl Eng Des*. 2017;323:269-279.
6. Voyagaki E, Kloukinas P, Dietz M, et al. Earthquake response of a multiblock nuclear reactor graphite core: experimental model vs simulations. *Earthq Eng Struct Dyn*. 2018;47(13):2601-2626.
7. Ensinger Technical Sheet. POM - Acetal Polyoxymethylene, TECAFORM Ensinger Plastics, www.ensinger.com
8. Ticona Celanese Technical Sheet. https://www.celanese.com/engineered-materials/engineered-materials.aspx
9. Driesner AR, Wagner P. Friction coefficients of graphite over the temperature interval 25°C to 2450°C. *J Appl Phys*. 1958;29(6):901-903.
10. Koziara T, Bićanić N. A distributed memory parallel multibody Contact Dynamics code. *Int J Numer Methods Eng*. 2011;87(1-5):437-456.
11. Martinuzzi P, Kudawool D, Koziara T, McLachlan N. *Verification, validation, comparison and visualization of whole core models (including SOLFEC and Parmec),* Proc. of 6th EdF Energy Nuclear Graphite Conference, Kendal, October 2018.
12. Kralj B, Humphreys SJ, Duncan BGJ. *Seismic Modelling of and AGR Nuclear Reactor Core,* Proc. of the ageing Management of Graphite Reactor Cores, University of Cardiff, 28-30 November, 193-200. 2005
13. Ahmed KM. The dynamic response of multi-layers AGR core brick arrays. *Nucl Eng Des*. 1987;104(1):1-66.
14. Moreau JJ. Numerical aspects of the sweeping process. *Comput Methods Appl Mech Eng*. 1999;177(3-4):329-349.
15. Jean M. The non-smooth contact dynamics method. *Comput Methods Appl Mech Eng*. 1999;177(3-4):235-257.

How to cite this article: Dihoru L, Oddbjornsson O, Cannell B, et al. Experimental and computational synergy for modelling an advanced gas-cooled reactor core under seismic excitation. *Earthquake Engng Struct Dyn*. 2020; 1–21. https://doi.org/10.1002/eqe.3291